Published online 15 December 2015

Nucleic Acids Research, 2016, Vol. 44, No. 2 ***969–982***
doi: 10.1093/nar/gkv1382

A novel RNA-binding mode of the YTH domain reveals the mechanism for recognition of determinant of selective removal by Mmi1

Chongyuan Wang, Yuwei Zhu, Hongyu Bao, Yiyang Jiang, Chao Xu, Jihui Wu* and Yunyu Shi*

Hefei National Laboratory for Physical Sciences at Microscale and School of Life Sciences, University of Science and Technology of China, Anhui 230027, China

Received September 28, 2015; Revised November 25, 2015; Accepted November 26, 2015

ABSTRACT

The YTH domain-containing protein Mmi1, together with other factors, constitutes the machinery used to selectively remove meiosis-specific mRNA during the vegetative growth of fission yeast. Mmi1 directs meiotic mRNAs to the nuclear exosome for degradation by recognizing their DSR (determinant of selective removal) motif. Here, we present the crystal structure of the Mmi1 YTH domain in the apo state and in complex with a DSR motif, demonstrating that the Mmi1 YTH domain selectively recognizes the DSR motif. Intriguingly, Mmi1 also contains a potential m^{6}A (N^6-methyladenine)-binding pocket, but its binding of the DSR motif is dependent on a long groove opposite the m^{6}A pocket. The DSR-binding mode is distinct from the m^{6}A RNA-binding mode utilized by other YTH domains. Furthermore, the m^{6}A pocket cannot bind m^{6}A RNA. Our structural and biochemical experiments uncover the mechanism of the YTH domain in binding the DSR motif and help to elucidate the function of Mmi1.

INTRODUCTION

Meiosis is a specialized cellular process that produces haploid gametes from diploid germ cells. Despite its biological significance, the molecular mechanism that controls meiosis remains largely unknown. Fission yeast *Schizosaccharomyces pombe* is an ideal model system for studying cellular entry into meiosis. In recent years, remarkable progress has been made in understanding the switch from mitosis to meiosis in *S. pombe*. During vegetative growth, the transcription of *S. pombe* meiotic genes is not completely repressed. In mitotic cells, to avoid impairments caused by the presence of unnecessary meiotic gene transcripts, *S. pombe* utilizes elimination machinery to remove these mRNAs. Mmi1, a YTH-family RNA-binding protein, plays an indispensable role in this process (1), together with nuclear poly(A)-binding protein Pab2 (2–4), Iss10 (5), Red1(6) and Red5 (7). In the RNA elimination process, Mmi1 binds the DSR motif specific for meiotic transcripts (1,8) and directs them to the exosome for degradation. Upon entering meiosis, Mmi1 is sequestered from the RNA elimination pathway into a dot-like nuclear body at the *sme2* locus via binding to Mei2 and a non-coding RNA (meiRNA) that also carries numerous DSR motifs, thereby facilitating the stable translation of meiotic gene transcripts (1,8,9). The RNA elimination machinery is also utilized to degrade several non-meiotic transcripts (10,11). In addition to its function in RNA elimination, Mmi1 also directs RNAi-dependent heterochromatin formation at meiotic genes *mei4* and *ssm4* via the Mmi1-DSR interaction as well as the recruitment of Red1 and the histone H3K9 methyltransferase Clr4 (12–14).

Recent studies have suggested that mammalian and budding yeast YTH family proteins selectively bind m^{6}A RNA (15–19). Structural characterizations have revealed that cage-like m^{6}A pockets, formed by conserved aromatic residues in the YTH domains, are utilized to preferentially accommodate the methyl group on m^{6}A (18,20–24). Thus, the possibility that the Mmi1 YTH domain might also bind m^{6}A RNA is intriguing. Mmi1-DSR interaction is crucial for RNA elimination and RNAi-dependent heterochromatin formation. However, the mechanism of specific targeting of DSR by Mmi1 remains unknown. To understand the molecular mechanism of this process, knowing the structure of the Mmi1 YTH domain in complex with a DSR motif at atomic resolution is essential. Here, we present the crystal structure of the Mmi1 YTH domain in the apo state and in complex with a DSR motif-containing RNA. This complex structure reveals a unique RNA-binding mode distinct from the m^{6}A RNA-binding mode utilized by other YTH domains, in which the RNA is bound in a long groove

*To whom correspondence should be addressed. Tel: +86 551 63607464; Fax: +86 551 63601443; Email: yyshi@ustc.edu.cn
Correspondence may also be addressed to Jihui Wu. Tel: +86 551 63603745; Fax: +86 551 63601443; Email: wujihui@ustc.edu.cn

opposite the putative m^{6}A-binding pocket of Mmi1. In addition, we found that the m^{6}A pocket of the Mmi1 YTH domain cannot bind m^{6}A RNA. Collectively, our work provides a structural basis for the specific recognition of DSR by Mmi1 and facilitates understanding that how the interaction between DSR and Mmi1 regulates switching from mitosis to meiosis.

MATERIALS AND METHODS

Protein and RNA preparations

The Mmi1 gene, which contains four introns, was amplified from the *S. pombe* genome. The introns were deleted via mutation using a MutanBEST kit (Takara), and the open reading frames (ORF) of Mmi1 were cloned into a modified pET28a (Novagen) vector without a protease cleavage site (p28a). The genes of human YTHDC1 (residues 344–509), human YTHDC2 (residues 1276–1430), human YTHDF2 (residues 394–562) and *S. cerevisiae* MRB1 (residues 141–306) were amplified from a human brain cDNA library and the *S. cerevisiae* genome, respectively, and subsequently cloned into p28a vectors. Mutants were generated using a MutanBEST kit (Takara) and verified by DNA sequencing. The proteins were expressed in *Escherichia coli* BL21 (DE3) cells (Novagen) cultured in LB medium at 37°C to OD_{600} = 0.8, then shifted to 16°C and induced with 0.4 mM IPTG for 24 h. The proteins were purified using an Ni-chelating resin (Qiagen) in 30 mM Tris (pH 8.0) and 1 M NaCl and then purified using a Superdex 75 column (GE Healthcare). RNA oligomers were purchased from Takara Bio, Inc. and dissolved in diethyl pyrocarbonate (DEPC)-treated water to a final concentration of 2 mM.

Isothermal titration calorimetry

ITC assays were carried out on a MicroCal iTC200 calorimeter (GE Healthcare) at 25°C. The buffer used for proteins and RNA oligomers was 50 mM Bis-Tris (pH6.8), 200 mM NaCl. The concentrations of proteins were determined spectrophotometrically. The RNA oligomers were diluted in the buffer to 10–25 μM. The ITC experiments involved 20 injections of 2 μl protein into 200 μl RNA. Reference measurements were carried out to compensate for the heat of dilution of the proteins. Curve fitting to a single binding site model was performed by the ITC data analysis module of Origin 7.0 (MicroCal) provided by the manufacturer. ΔG° of protein–RNA binding was computed as $-RT\ln(1/K_D)$, where R, T and K_D are the gas constant, temperature and dissociation constant, respectively. The thermodynamic parameters of the ITC experiments are listed in Supplementary Table S1.

Crystallization, data collection and structure determination

YTH^{Mmi1} (residues 322–488) was concentrated to ∼10 mg/ml in a buffer consisting of 15 mM Bis-Tris (pH6.8), 200 mM NaCl, 1 mM EDTA and 1 mM DTT. The YTH^{Mmi1}-CUUAAACC complex was prepared by mixing 10 mg/ml protein (the final concentration) with the 8-mer RNA 5′-CUUAAACC-3′ at a molar ratio of 1:1.5. The crystals of YTH^{Mmi1} and the YTH^{Mmi1}-CUUAAACC complex were grown at 293 K via the hanging drop method, with the mother liquor containing 100 mM MES (pH 6.0) and 18% (w/v) PEG 2000. X-ray diffraction data for the crystals were collected on beamline 17U1 of the Shanghai Synchrotron Radiation Facility (SSRF). The data were processed using HKL2000 software. The structure of YTH^{Mmi1} was determined by molecular replacement in the program MOLREP (25) using the structure of YTH^{YTHDC1} (PDB ID: 4R3H) as the search model. The structure of the YTH^{Mmi1}-CUUAAACC complex was also determined by molecular replacement, using the structure of YTH^{Mmi1} as the search model. The models were subsequently refined by the programs REFMAC5 (26) and COOT (27). The R_{work} and R_{free} of the YTH^{Mmi1} structure were refined to 21.2% and 25.6%, respectively. The R_{work} and R_{free} of the YTH^{Mmi1}-CUUAAACC complex were refined to 17.6% and 21.6%, respectively. Data collection and refinement statistics are listed in Supplementary Table S2. The structure figures were prepared in PyMOL (28).

Coordinates

Coordinates and structure factors for YTH^{Mmi1} and the YTH^{Mmi1}-CUUAAACC complex have been deposited in the Protein Data Bank (PDB) under the accession codes 5DNP and 5DNO, respectively.

RESULTS

The Mmi1 YTH domain binds the DSR motif

A previous study revealed that the YTH domain is essential for Mmi1 binding of the DSR motif (8), but a comprehensive investigation of the Mmi1-DSR interaction is lacking. To investigate the Mmi1-DSR interaction quantitatively, we measured the binding affinities of the Mmi1 YTH domain for the DSR motif and mutant motifs by isothermal titration calorimetry (ITC). First, we mapped the YTH domain function of DSR motif-binding by measuring the binding affinities of a DSR motif-containing 10-mer RNA (5′-CCUUAAACCU-3′) for Mmi1 proteins with different boundaries (Figure 1A). Mmi1$^{316–488}$ and Mmi1$^{322–488}$ bind the 10-mer RNA with similar dissociation constants (K_D = 0.39 ± 0.01 μM and 0.44 ± 0.03 μM, respectively), while Mmi1$^{338–488}$ binds the 10-mer RNA with a K_D > 30 μM and no binding was detected between the 10-mer RNA and Mmi1$^{345–488}$ (Figure 1B). The ITC results suggest that Mmi1$^{322–488}$ (hereafter referred to as YTH^{Mmi1}) is the minimum region required for strong DSR binding. To study the sequence specificity of YTH^{Mmi1}-RNA binding, we measured the affinities of YTH^{Mmi1} for 10-mer RNAs with single-point mutations. $U_{+1}G$, $A_{+3}G$, $A_{+5}G$ and $C_{+6}G$ mutant RNAs bind to YTH^{Mmi1} ∼7.9-fold, >67-fold, >44-fold and ∼8.3-fold weaker than the wild-type RNA, respectively (Figure 1C). $U_{+2}A$, $U_{+2}C$ and $U_{+2}G$ mutant RNAs do not alter the binding of YTH^{Mmi1} significantly (Figure 1D). No interaction was detected between the $A_{+4}G$ mutant RNA and YTH^{Mmi1} (Figure 1C). Taken together, our ITC results suggest that YTH^{Mmi1} binds the DSR motif with specificity at positions +1, +3, +4, +5 and +6, but with only a slight preference for U at position +2.

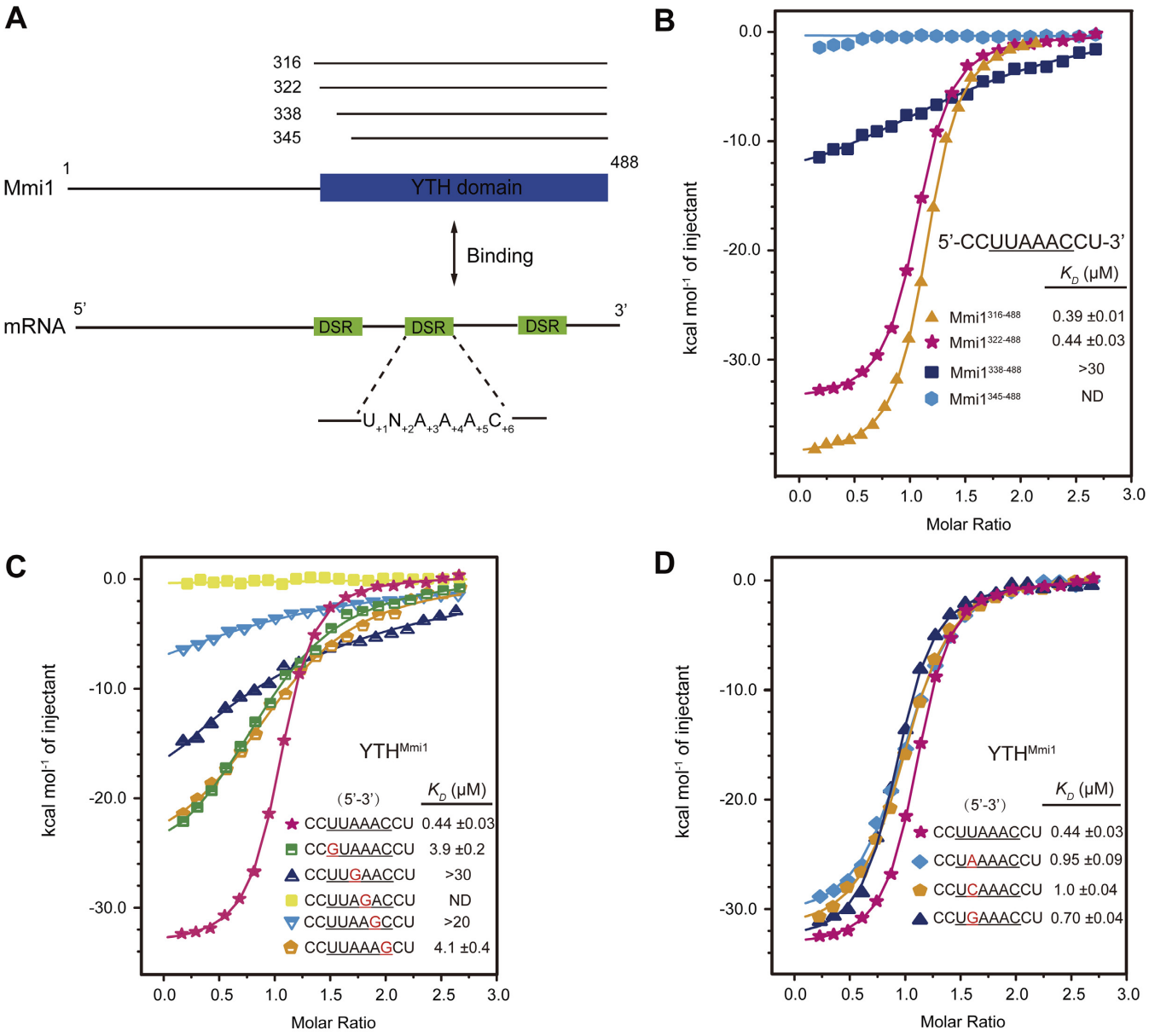

Figure 1. The Mmi1 YTH domain binds the DSR motif. (**A**) The domain architecture of Mmi1and DSR. Black lines represent the Mmi1 constructs used for ITC and structural studies. (**B**) The ITC fitting curves of 10-mer RNA 5′-CCUUAAACCU-3′ to Mmi1 proteins. The complete thermodynamic parameters for all ITC titrations are listed in Supplementary Table S1. (**C**–**D**) The ITC fitting curves of mutant 10-mer DSR RNAs to YTH^{Mmi1}.

Overall structure of the YTH^{Mmi1}-CUUAAACC complex

To provide structural insight into the selective recognition of the DSR motif by the YTH^{Mmi1}, we sought to determine the structure of the complex by X-ray crystallography. After screening DSR-containing RNAs of different lengths, we obtained the co-crystal of YTH^{Mmi1}with an 8-mer RNA (5′-CUUAAACC-3′) and determined its structure at a resolution of 1.8 Å (Supplementary Table S2). The 9-mer RNAs 5′-CCUUAAACC-3′ and 5′-CUUAAACCU-3′ displayed similar binding affinities for YTH^{Mmi1} (K_D = 1.1 ± 0.02 μM and 1.2 ± 0.03 μM, respectively), and the 8-mer RNA binds to YTH^{Mmi1} ∼3-fold weaker than did the 10-mer RNA (K_D = 1.8 ± 0.1 μM) (Supplementary Table S1). When we trimmed the 8-mer RNA further to a 6-mer RNA by removing one nucleotide at each end, the binding affinity further decreased ∼6-fold (K_D = 8.3 ± 2 μM). Therefore, we surmised that our 8-mer RNA complex maintains a strong binding affinity that could reflect the sequence selectivity revealed by ITC binding experiments. In addition, we determined the structure of apo YTH^{Mmi1} at 2.2 Å and compared it with the structure of the RNA complex (Supplementary Table S2).

YTH^{Mmi1}adopts a typical YTH fold with a core of five β-sheet strands (β1-β5) packed by four helixes (α1–α4) (Supplementary Figure S1A). Structural comparisons with previously characterized YTH domains reveal high similarities between these YTH domains (with r.m.s deviations for C_α

atoms of 0.95 Å, 1.3 Å and 1.6 Å compared with YTH domains of YTHDC1, YTHDF2 and MRB1, respectively). In the complex structure, electronic densities corresponding to the first seven nucleotides were easily traced (i.e. nucleotides C_0, U_{+1}, U_{+2}, A_{+3}, A_{+4}, A_{+5} and C_{+6}, respectively)(Figure 2A and B). The RNA adopts an extended conformation and lies in the groove composed of the N-terminal loop, α1, α4, β1, β3–β5 and the C-terminal loop of YTH^{Mmi1} (Figure 2A and B). The groove regions contacting C_0-U_{+2} and C_{+6} are positively charged, whereas the rest of the RNA-binding groove is hydrophobic (Figure 2B). U_{+1}inserts into a positively charged pocket (the U_{+1} pocket) formed by α1, α4, β4, β5 and the C-terminus of YTH^{Mmi1} (Figure 2A and B). The phosphate backbones of U_{+1} and U_{+2} interact with a positively charged surface formed by α4, β3 and β4 (Figure 2A and B). A_{+3}, A_{+4}, A_{+5} and C_{+6} interact with the hydrophobic surface and the positive segment comprised of the N-terminal loop, β1, β3 and α4, and their bases are successively packed (Figure 2A, B and C). In the asymmetric unit, the bases of C_0 and U_{+2} do not interact with YTH^{Mmi1} directly(Figure 2B and C). Notably, C_0 and U_{+2} participate in crystallization packing via their contacts with another YTH^{Mmi1} molecule (Supplementary Figure S2A).

RNA binding induces conformational changes in the N- and C-termini of YTH^{Mmi1}

Comparison of the apo and RNA-bound structures reveals dramatic conformational changes in the N-terminus and C-terminus of YTH^{Mmi1} induced by RNA binding (Supplementary Figure S2B). The N-terminus (residues 322–338) and C-terminus (residues 483–488) are not visible in the apo structure of YTH^{Mmi1}, indicating flexible conformations. In the RNA-bound structure, the N- and C-termini of YTH^{Mmi1} fold into two loops and interact extensively with U_{+1}, A_{+5} and C_{+6} (Supplementary Figure S2B). The interaction between RNA and the N-terminal loop is also consistent with the ITC result indicating that $Mmi1^{345–488}$ lacking the N-terminal loop cannot bind to the 10-mer DSR motif. The conformation of the N-terminal loop is stabilized by the hydrogen bonding networks of residues R331 and S333 (Supplementary Figure S2B). Mutations of R331 and S333 to alanine significantly decrease the binding affinity of YTH^{Mmi1}-RNA (∼3.3-fold and ∼13-fold; Supplementary Table S1), reinforcing the importance of the N-terminal loop formation in RNA recognition.

Recognition of U_{+1}

The U_{+1} uracil is anchored in the U_{+1} pocket via three hydrogen bonds from the main-chain atoms of T437 in β5 and D487 in the C-terminal loop of YTH^{Mmi1}: the N^3H group of U_{+1} to the main chain carbonyl of T437, the main chain NH groups of T437 and D487 to the O^2 and O^4 oxygens of U_{+1}, respectively (Figure 3A and B). In addition to these hydrogen-bonding interactions, the side chains of I480 and R488 also contribute to hydrophobic interactions and π–π packing with the uracil of U_{+1}, respectively (Figure 3A). These hydrogen bonds make U_{+1} recognition highly specific because substitution of U_{+1} with any other nucleotides ablates the hydrogen bonds or introduces steric clashes with T437 and D487 (Figure 3C). Consistently, the binding affinities of U_{+1}G, U_{+1}A and U_{+1}C mutant 10-mer DSR RNAs to YTH^{Mmi1} are ∼7.9-fold, ∼9.0-fold and ∼29-fold weaker than that of wild-type 10-mer DSR RNA, respectively (Figure 3D).

Recognition of A_{+3} and A_{+4}

A_{+3} and A_{+4} are bound in the hydrophobic surface composed of Y466, S470, C473 and N477 of α4; S350 and Y352 of β1; Y392 of β3; Y406 of β4; and I435 of β5 (Figures 2B and 4A and B). A_{+4} participates in base packing with A_{+3} and A_{+5} at a distance of 3.5 Å, respectively (Figure 4A). The N^1 nitrogen of A_{+3} makes a hydrogen bond with the OH group of Y352, and the adenine ring of A_{+3} forms hydrophobic interactions with the side chains of Y392 and C473 (Figure 4B). The N^1 nitrogen of A_{+4} makes a hydrogen bond with the OH group of Y466, and the N^4 nitrogen of A_{+4} forms a water-mediated hydrogen bond with the OH groups of S350 and Y392 (Figure 4B). In addition, the C'4-ribosyl oxygen of A_{+3} forms another hydrogen bond with the side chain NH group of N477 (Figure 3A). Replacing A_{+3} and A_{+4} with any other nucleotides would disrupt the hydrogen bond from Y352 or Y466 (Supplementary Figure S3A and B). Furthermore, the substitution of A_{+3} or A_{+4} with G would also introduce a steric clash to Y392 or Y466 (Supplementary Figure S3A and B). Consistently, the binding of A_{+3}U, A_{+3}C, A_{+3}G and A_{+4}C mutant 10-mer DSR RNAs to YTH^{Mmi1} are ∼12-fold, ∼29-fold, >67-fold and >67-fold weaker than that of wild-type 10-mer DSR RNA, respectively (Figure 4C and D), and the mutation of A_{+4} to U or G abrogates the interaction (Figure 4D).

Recognition of A_{+5} and C_{+6}

A_{+5} and C_{+6} are recognized by the N-terminal loop of YTH^{Mmi1} (Figures 2A and 5A and B). The uracil of C_{+6} packs against the adenine of A_{+5} at a distance of 3.8 Å (Figure 5A). The N^1 nitrogen of A_{+5} makes a hydrogen bond with the NH_2 group of N336, and the O^2 oxygen of C_{+6} forms two hydrogen bonds with the guanidino group of R338 (Figure 5B). Mutating A_{+5} to any other nucleotide disrupts its hydrogen bonding with N336 (Supplementary Figure S3C). Indeed, the binding of A_{+5}C, A_{+5}U and A_{+5}G mutant 10-mer DSR RNAs to YTH^{Mmi1} are ∼7.9-fold, ∼13-fold and >44-fold weaker than that of wild type 10-mer DSR RNA, respectively (Figure 5C). Mutation of C_{+6} to G abolishes the two hydrogen bonds formed with R338, and replacing of C_{+6} with U or A also disrupts one of the hydrogen bonds (Supplementary Figure S3D). Consistently, C_{+6}U, C_{+6}A and C_{+6}G mutations in RNA weakened the interaction with YTH^{Mmi1} by ∼3.8-fold, ∼3.4-fold and ∼8.3-fold (Figure 5D).

To evaluate the roles of the YTH^{Mmi1} residues in binding the DSR motif (Figure 2C), we performed mutagenesis experiments and assessed the binding of the mutants to the 10-mer RNA (5′-CCUUAAACCU-3′) by ITC experiments. Mutations in the RNA-binding residues severely impair YTH^{Mmi1}-RNA binding, reinforcing the YTH^{Mmi1}-RNA interactions observed in the complex structure (Supplementary Table S1).

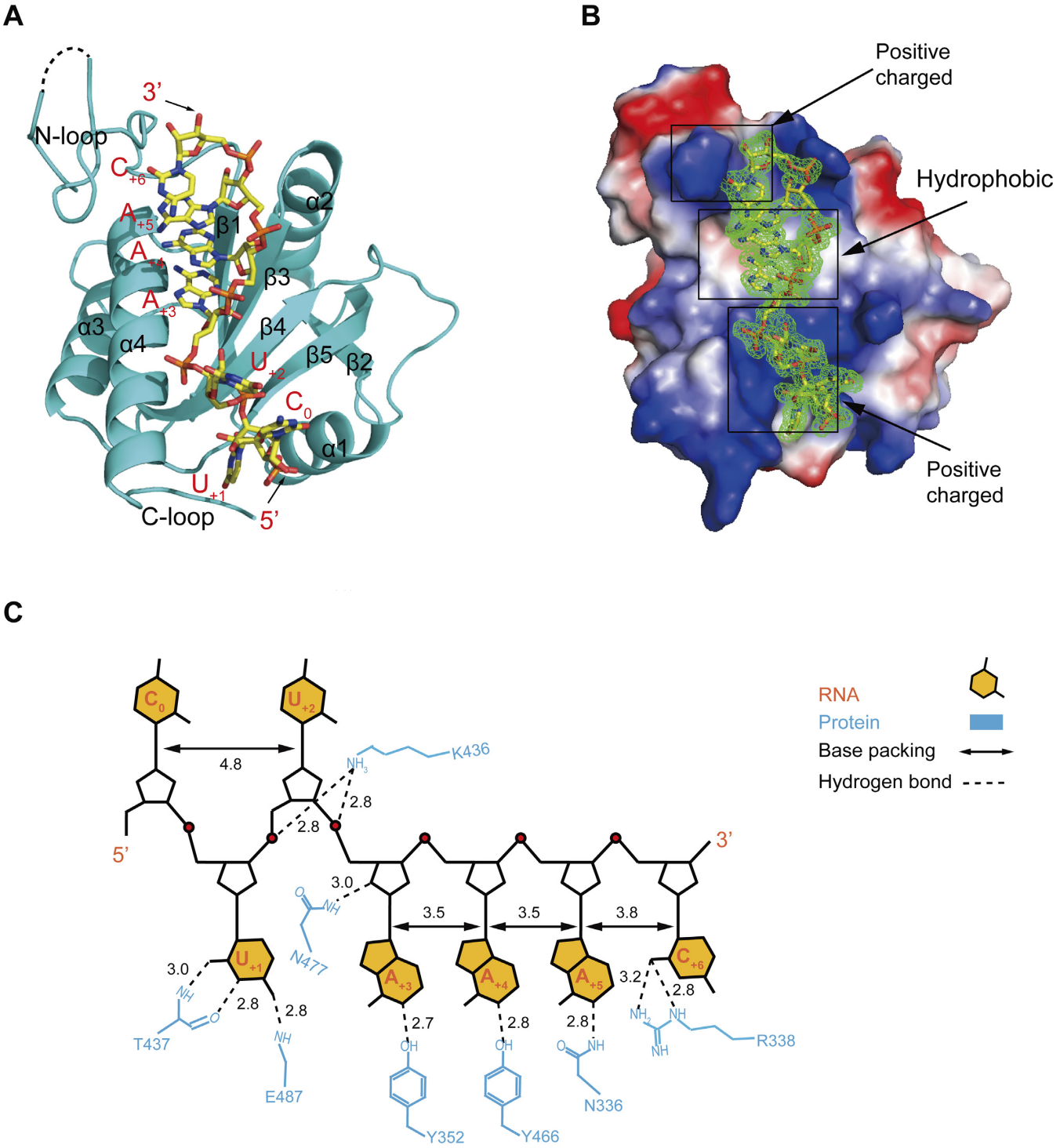

Figure 2. Structure of YTH^{Mmi1}-CUUAAACC complex. (**A**) An overall view of the complex structure. Residues 326–329 are invisible in the density map and are indicated by the dashed black line. (**B**) The electrostatic potential of the YTH^{Mmi1}-CUUAAACC complex surface, in which positively charged, negatively charged and neutral areas are represented in blue, red and white, respectively. The F_o-F_c stimulated annealing omit map of the RNA was contoured at +3.0 σ. (**C**) Schematic representations of the recognition of RNA (yellow) by YTH^{Mmi1} (cyan).

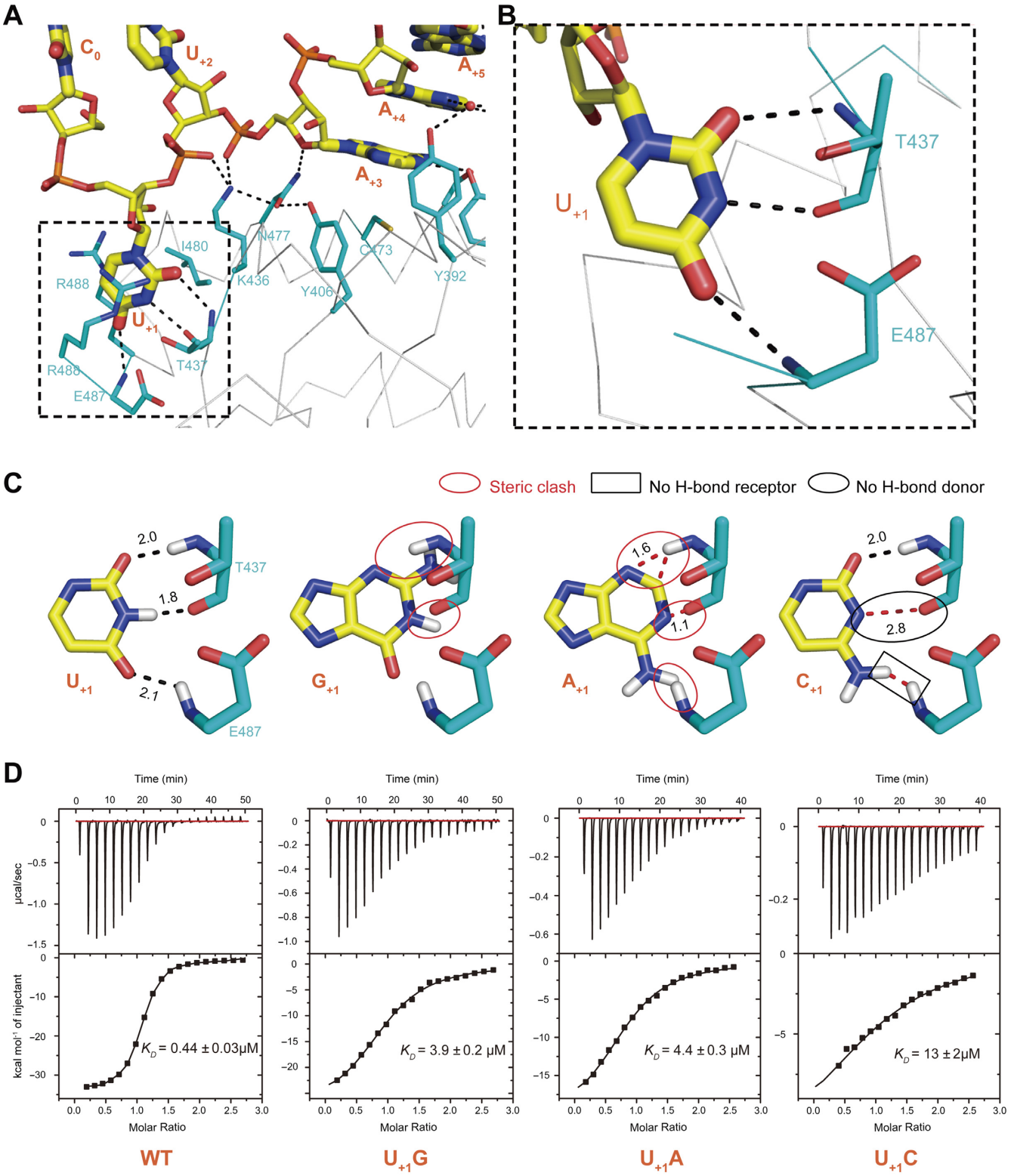

Figure 3. Recognition of U_{+1}. (**A** and **B**) Interactions of U_{+1} with Mmi1. Hydrogen bonds are indicated in black dashes. (**C**) Models for U_{+1} mutants. The polar hydrogen atoms in the binding interface are shown as grey sticks. Black dashed lines indicate the hydrogen bonds. Red dashed lines indicate the distances between atoms without hydrogen bonding interactions. The steric clash is highlighted with red ovals, while the loss of hydrogen bonds is highlighted with black ovals and black rectangles. (**D**) The ITC fitting results of YTH^{Mmi1} with wild type and mutant 10-mer RNAs at +1 position.

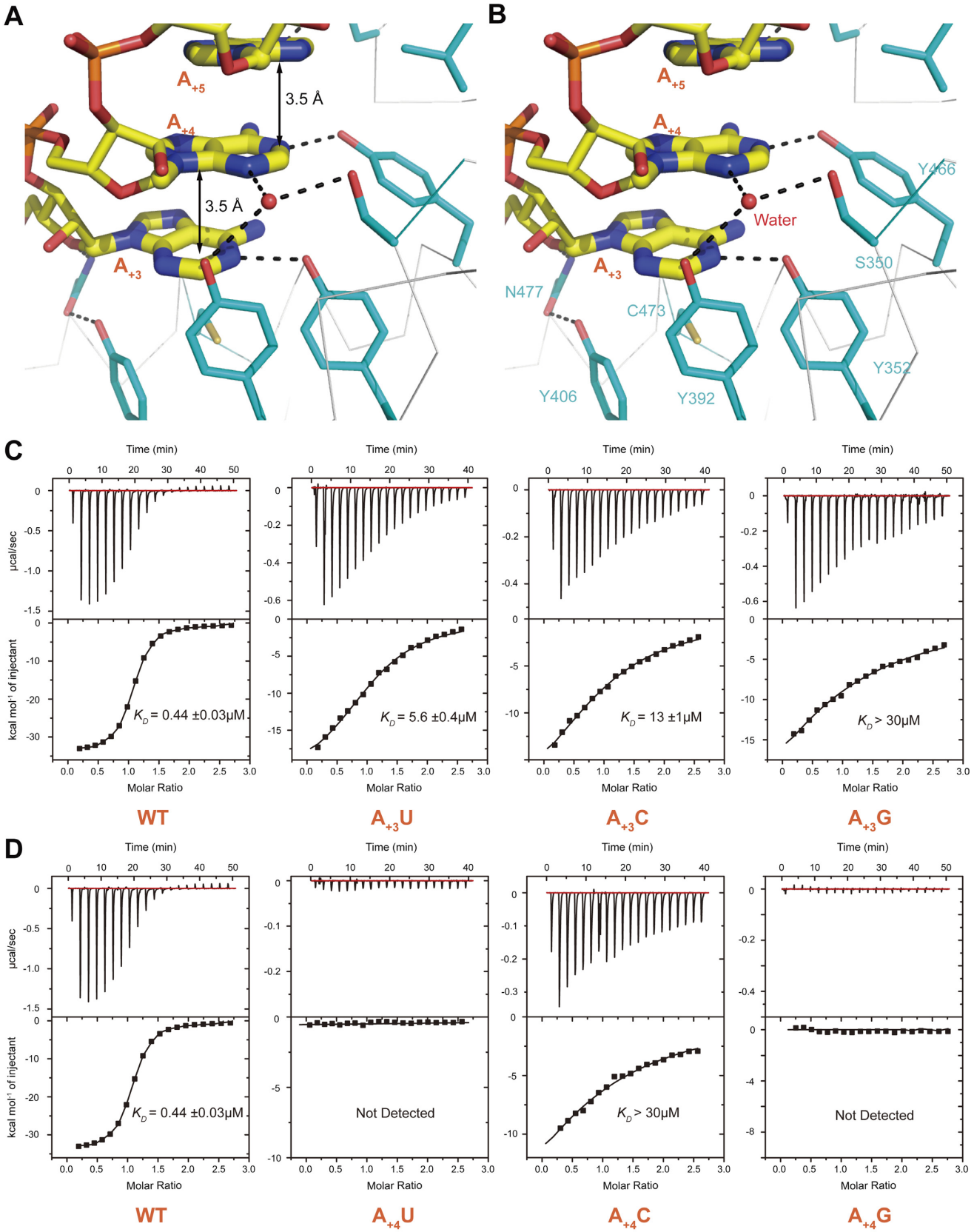

Figure 4. Recognition of A_{+3} and A_{+4}. (**A** and **B**) Interactions of A_{+3} and A_{+4} with Mmi1. Hydrogen bonds are indicated as black dashes. (**C** and **D**) The ITC fitting results for YTH^{Mmi1} with wild type and mutant 10-mer DSR RNAs at the +3 or +4 position.

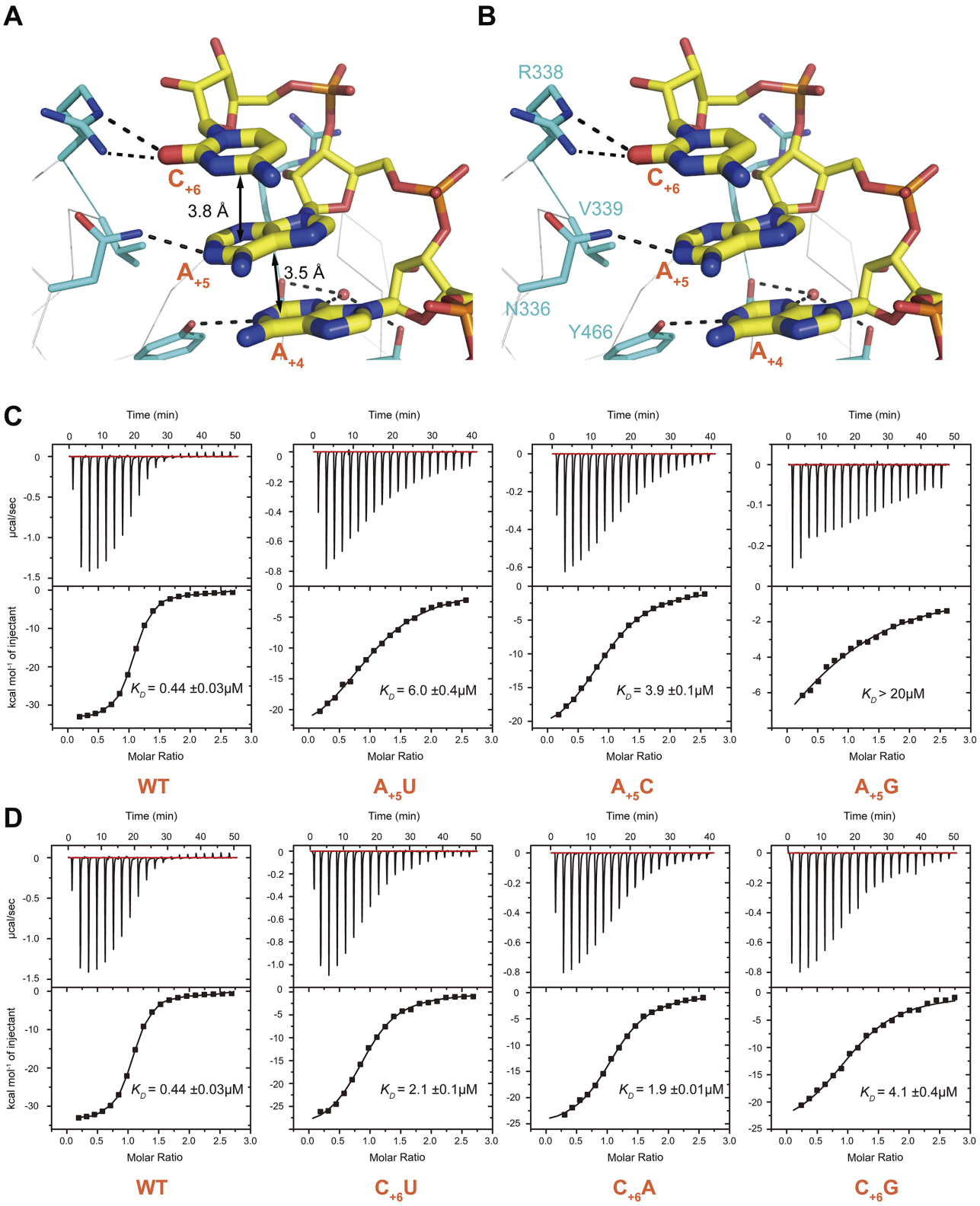

Figure 5. Recognition of A_{+5} and C_{+6}. (**A** and **B**) Interactions of A_{+5} and C_{+6} with Mmi1. Hydrogen bonds are indicated as black dashes. (**C** and **D**) The ITC fitting results of YTH^{Mmi1} with wild type and mutant 10-mer DSR RNAs at the +5 or +6 position.

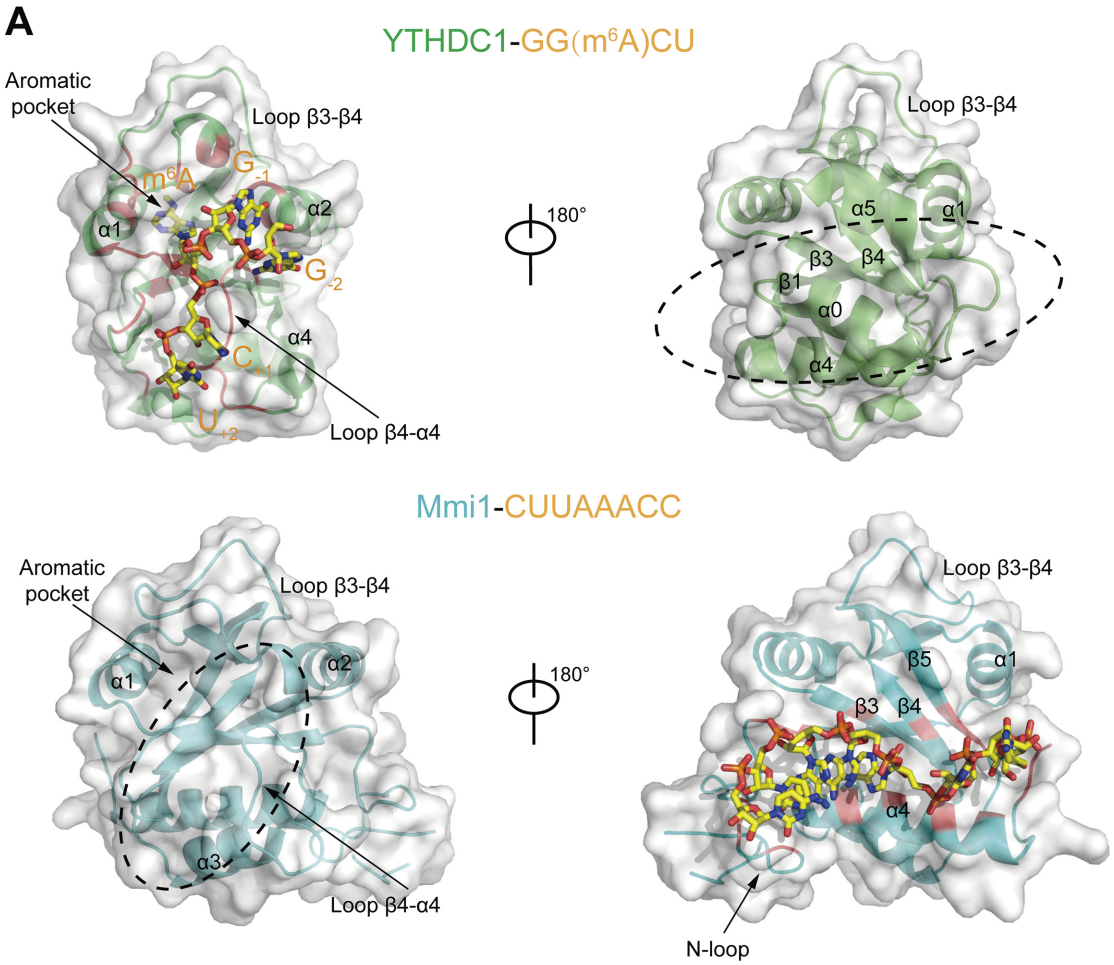

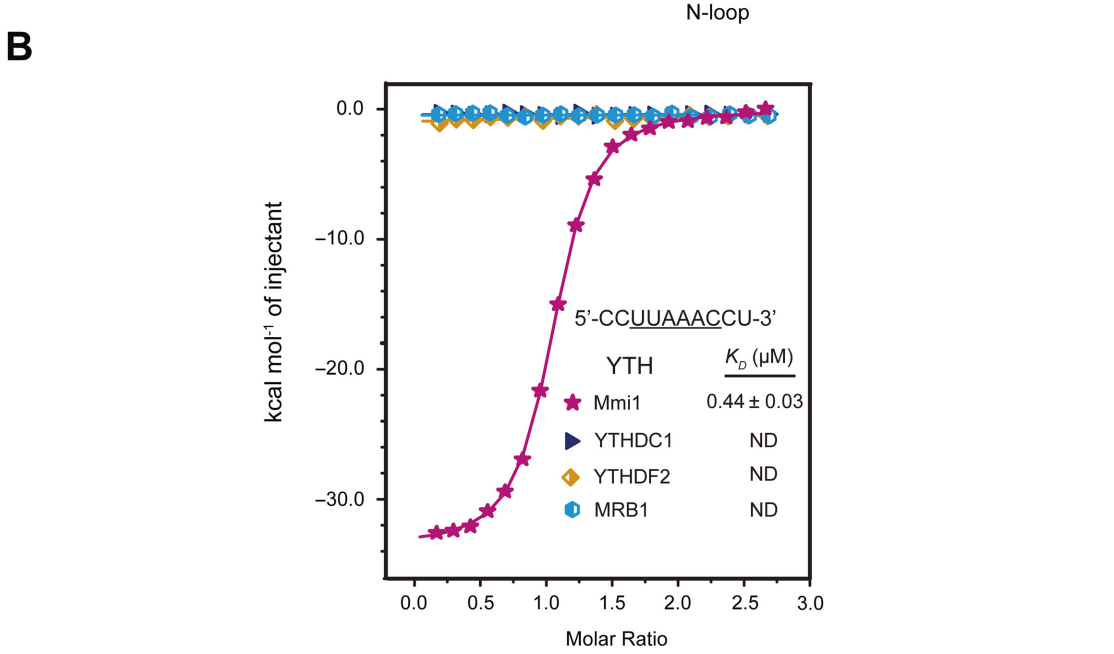

Figure 6. Comparison of the RNA binding mode of Mmi1 and other YTH domains. (**A**) A comparison of RNA binding by YTH^{YTHDC1} (PDB: 4R3I) and YTH^{Mmi1}. The cartoons of YTH^{YTHDC1} and YTH^{Mmi1} are colored in green and cyan, and the RNA-binding regions are in red. The aromatic pockets and structural elements participating in RNA-binding are highlighted. (**B**)The ITC fitting curves of 10-mer DSR RNA (5′-CCUUAAACCU-3′) binding to the YTH domains.

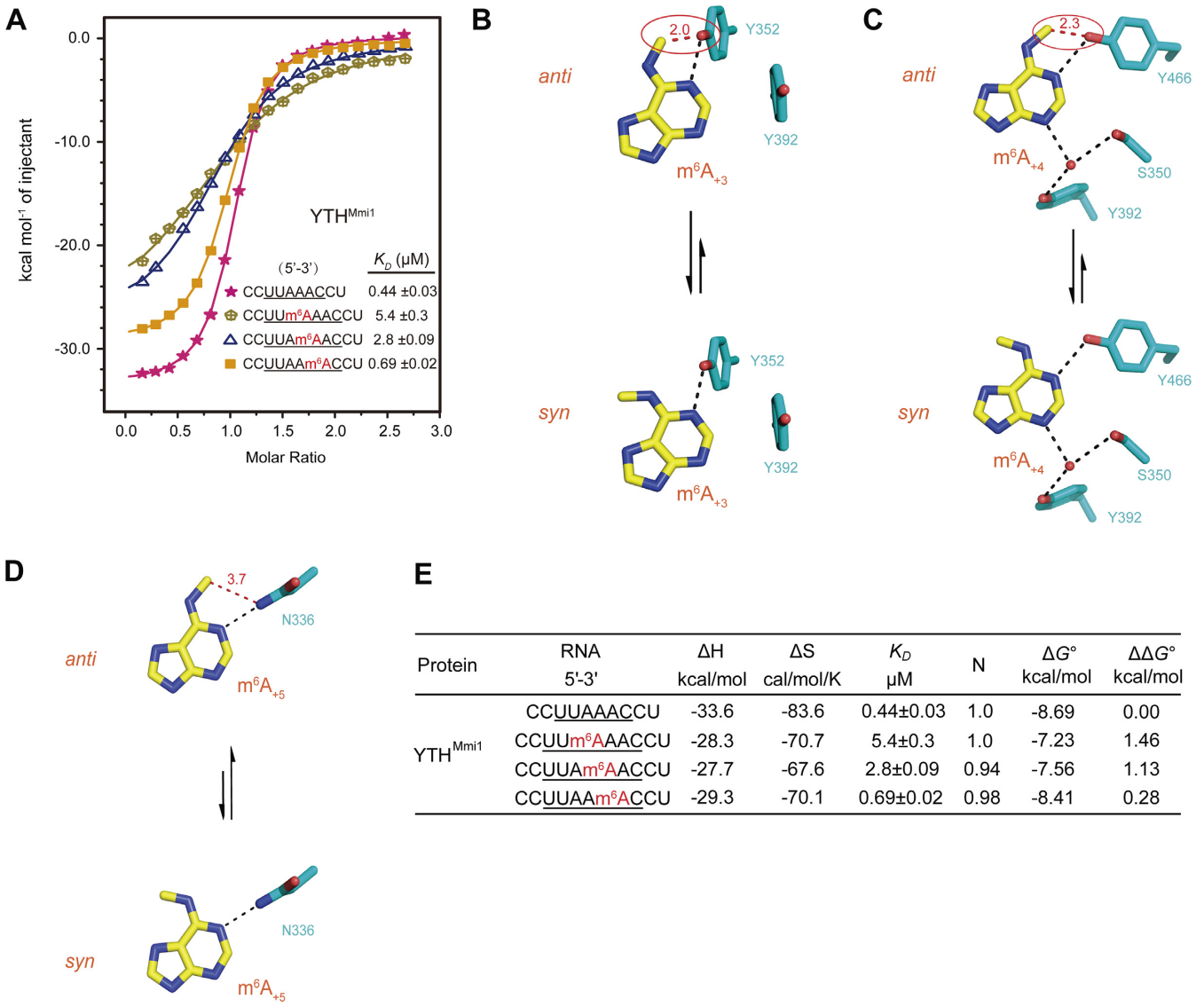

E

Protein	RNA 5'-3'	ΔH kcal/mol	ΔS cal/mol/K	K_D μM	N	ΔG° kcal/mol	ΔΔG° kcal/mol
YTH^{Mmi1}	CCUUAAACCU	-33.6	-83.6	0.44±0.03	1.0	-8.69	0.00
	CCUUm^{6}AAACCU	-28.3	-70.7	5.4±0.3	1.0	-7.23	1.46
	CCUUAm^{6}AACCU	-27.7	-67.6	2.8±0.09	0.94	-7.56	1.13
	CCUUAAm^{6}ACCU	-29.3	-70.1	0.69±0.02	0.98	-8.41	0.28

Figure 7. Methylation of the DSR motif weakens Mmi1 binding. (**A**) ITC fitting curves of YTH^{Mmi1} to unmodified and methylated 10-mer DSR RNAs. (**B**, **C** and **D**) Structural models of m^{6}A$_{+3}$, m^{6}A$_{+4}$ and m^{6}A$_{+5}$, in *syn* and *anti* conformations. Red dashed lines indicate the distances between atoms, and the steric clashes are highlighted with red ovals. (**E**) The thermodynamic parameters of the ITC fitting curves in Figure 7A.

A new RNA binding mode

Several YTH domain complexes have been determined to be readers of m^{6}A RNA, which prompted us to compare our structure with other m^{6}A RNA complexes. Here, we superimposed our complex with the reported YTHDC1 complex and found that although the structures of the two proteins could be superimposed with high agreement, the binding characteristics of the two complexes were distinct. The two YTH domains bind to their respective RNA molecules via two different surfaces. YTHDC1 recognizes GGm^{6}ACU in a groove comprised of β1, loop β1-α1, α1, β2 and loop β3-β4 (Figure 6A), whereas YTH^{Mmi1} binds to the DSR motif via a long groove involving the N-terminal loop, α1, α4, β1, β3-β5 and the C-terminal loop, which opposes the region corresponding to the m^{6}A RNA-binding interface in YTHDC1 (Figure 6A). Even if YTH^{Mmi1} also contains a potential m^{6}A-binding pocket, its binding to the DSR motif is independent of the m^{6}A pocket (Figure 6A). Furthermore, our ITC results showed that the YTH domains of YTHDC1, YTHDF2 and MRB1 cannot bind the 10-mer DSR RNA (Figure 6B). Thus, our complex structure represents a previously unreported RNA binding mode for YTH domains.

DISCUSSION

Mmi1 is a controller of meiotic entry unique to fission yeast

In mitotic *S. pombe* cells, Mmi1 controls meiosis entry via the selective elimination of meiosis-specific mRNA. Once switching to the meiotic cycle, Mei2 and meiRNA bind to Mmi1 and sequester it from the RNA elimination pathway, thereby permitting meiotic progression. The Mmi1-

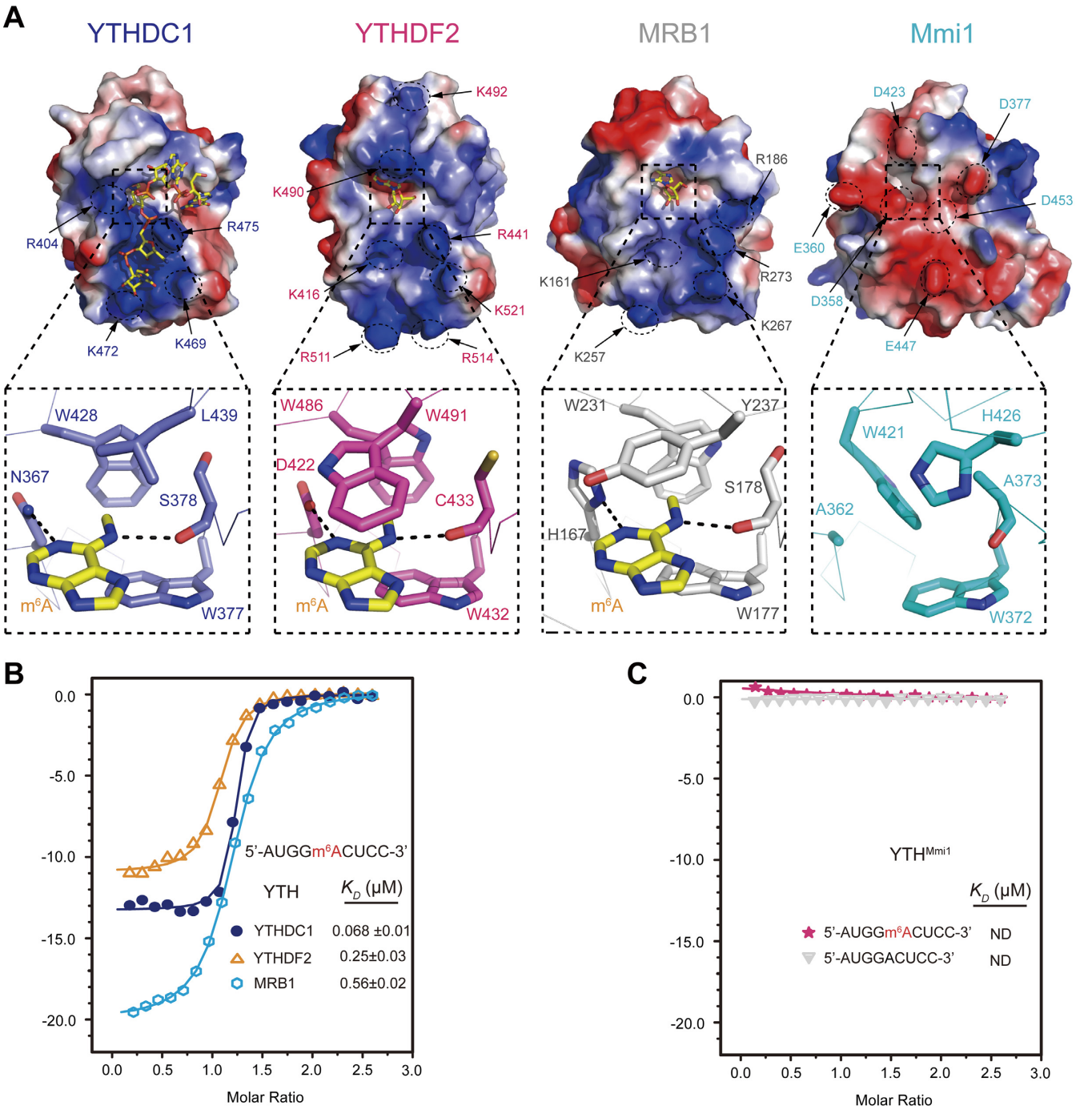

Figure 8. Detailed comparisons of the aromatic cages and the surrounding grooves of YTH domains. (**A**) The aromatic cages and the surrounding grooves of the YTH domains. The YTH^{YTHDC1}-GGm^{6}ACU complex (PDB: 4R3I), YTH^{YTHDF2}-m^{6}A complex (PDB: 4RDN) and YTH^{MRB1}-m^{6}A complex (PDB: 4RCM) are aligned to YTH^{Mmi1}. The upper pictures show the electrostatic potential of the surface, in which positively charged residues in the m^{6}A RNA-binding interfaces of YTHDC1, YTHDF2 and MRB1 as well as the negatively charged residues near the aromatic cage of Mmi1 are indicated. The lower pictures are enlarged views of the aromatic cages. (**B**) The ITC fitting curves of the m^{6}A RNA (5′-AUGGm^{6}ACUCC-3′) to the YTH domains of YTHDC1, YTHDF2 and MRB1. (**C**) The ITC fitting curves of the m^{6}A RNA and the unmethylated counterpart to the YTH domains of Mmi1.

meiRNA complex is also dependent on the numerous DSR motifs present in meiRNA. Our study explains how the DSR motif is selectively recognized by Mmi1 on a structural level. We have also demonstrated that the DSR motif cannot be recognized by the human YTH proteins YTHDC1 and YTHDF2, as well as the *S. cerevisiae* YTH protein MRB1 (Figure 6B). In YTHDC1, YTHDF2 and MRB1 structures, their potential DSR-binding grooves are occupied by the N-terminal segments of those YTH domains, which form helix α0 in YTHDC1 or N-loops in YTHDF2 and MRB1 (Supplementary Figure S4). Furthermore, the DSR-binding residues are strictly conserved in Mmi1 homologues in fission yeast (i.e. *S. pombe*, *S. japonicus*, *S. octosporus* and *S. cryophilus*), whereas most residues are not conserved in budding yeast or mammalian YTH proteins (Supplementary Figure S1C). Collectively, our data suggest that DSR-binding property is unique for fission yeast Mmi1 proteins. In contrast to the meiotic entry regulatory function of Mmi1, MRB1 has been suggested to play a role in meiosis progression in *S. cerevisiae* (19). Thus, the YTH proteins in budding and fission yeasts seem to have evolved opposite functions in meiosis from the common ancestor of both yeasts.

Methylation of the DSR motif weakens Mmi1 binding

The N^1 nitrogen atoms of A_{+3}, A_{+4} and A_{+5} in the DSR motif form hydrogen bonds with Y352, Y466 and N336, respectively (Figure 2C). Deletion of any one of these hydrogen bonds severely impairs DSR RNA binding to the Mmi1 YTH domain (Supplementary Table S1). Does methylation of the N^6 nitrogen atoms of adenosine nucleotides affect the hydrogen bonding of neighboring N^1 nitrogen atoms? To address this question, we measured the binding affinities of YTH^{Mmi1} with 10-mer DSR RNAs that had been N^6-methylated at positions A_{+3}, A_{+4} and A_{+5}, respectively. N^6-methylation of A_{+3} and A_{+4} weaken YTH^{Mmi1}-DSR binding by ∼11-fold and ∼5.5-fold (Figure 7A), whereas N^6-methylation of A_{+4} leads to only a ∼0.57-fold decrease in binding affinity (Figure 7A).

The N^6-methyl group on adenosine exists in *syn* and *anti* conformations in solution, and the *syn* conformation is energetically favored by ∼1.5 kcal/mol over the *anti* conformation (29). If the N^6-methyl group of A_{+3} or A_{+4} is accommodated in the *anti* conformation, it would severely clash with residue Y352 or Y466 (Figure 7B and C). To avoid steric clashes, the N^6-methyl group on A_{+3} or A_{+4} must rotate into the high-energy *syn* conformation (Figure 7B and C), which results in the destabilization of YTH^{Mmi1}-DSR binding and decreases in binding affinities. The N^6-methyl group of A_{+5} can be accommodated in the low-energy *anti* conformation without steric clashes (Figure 7D); thus, methylation of A_{+4} leads to only a 0.57-fold decrease in binding affinity (Figure 7A). The destabilization energies ($\Delta\Delta G^\circ = \Delta G^\circ_{\text{Methylated RNA}} - \Delta G^\circ_{\text{WT RNA}}$) of A_{+3}- and A_{+4}-methylation are 1.46 kcal/mol and 1.13 kcal/mol, respectively (Figure 7E), consistent with the conformational transition energy from *anti* to *syn* of the N^6-methyl group (∼1.5 kcal/mol). m^6A modification were shown to assist RNA binding by proteins (such as YTHDC1, YTHDF2 and MRB1) and influence RNA stability and structure (30). Although our data were obtained *in vitro*, it implies that m^6A methylation of RNA may impede its binding to some proteins *in vivo*.

The m^6A pocket of Mmi1 cannot bind m^6A RNA

The m^6A RNA-binding YTH domains utilize m^6A pockets to accommodate the methyl group of m^6A, which form cages of aromatic residues (Figure 8A). These specific interactions between m^6A RNA and YTH domains were further validated via ITC assay using a 9-mer m^6A RNA (5′-AUGGm^6ACUCC-3′) as the target RNA, which contains a consensus m^6A motif of GGm^6AC. The m^6A RNA binds the YTH domains of YTHDC1, YTHDF2 and MRB1 with K_D values of 0.068 ± 0.01 μM, 0.25 ± 0.03 μM and 0.56 ± 0.02 μM, respectively (Figure 8B). The m^6A pocket is also conserved in Mmi1 (Figure 8A). To test whether this pocket binds m^6A RNA, we utilized the ITC assay to detect the interaction of the Mmi1 YTH domain with the 9-mer m^6A RNA and the unmethylated counterpart. However, the Mmi1 YTH domain did not bind the m^6A RNA or the unmethylated RNA (Figure 8C).

To understand the structural origin of why the Mmi1 m^6A pocket cannot bind the m^6A RNA, we carried out a detailed comparison of the m^6A pocket with those of other YTH domains. In the YTHDC1-RNA complex, the N^1 nitrogen of m^6A is hydrogen bonded to N367, while the corresponding residue in Mmi1 is an alanine (A362), which may weaken the binding of m^6A (Figure 8A). The nucleotides flanking m^6A are accommodated by the positively charged groove of YTHDC1 (Figure 8A), and the corresponding regions of YTHDF2, YTHDC2 and MRB1 are also rich with positively charged residues (Figure 8A and B, Supplementary Figures S4 and S6). However, the region surrounding the aromatic cage of Mmi1 is rich in negatively charged residues (D358, D360, D423, E441 and D453), which would generate severe repulsions if the m^6A RNA binds the groove (Figure 8A). The charge repulsions would abolish the binding of m^6A RNA to the m^6A pocket of Mmi1 YTH domain.

RNA m^6A methylation is likely to be lost in fission yeast

m^6A is the most prevalent modification of the mRNA and long noncoding RNA of most eukaryotes, from budding yeast, plants and flies to mammals (31), whereas the m^6A methylation of RNA has not been reported in fission yeast. It is intriguing to note that m^6A RNA methylation also exists in fission yeast. From budding yeast to mammals, the YTH-family proteins function as m^6A readers (31). However, we found that Mmi1, the only YTH-family protein in fission yeast, cannot bind the consensus m^6A motif GGm^6AC. Furthermore, homologues of the m^6A RNA methyltransferases METTL3 and METTL14 seem to be absent in fission yeast (32). The absence of m^6A writers and readers implies the loss of m^6A RNA modification fission yeast.

ACCESSION NUMBERS

PDB IDs: 5DNP and 5DNO.

SUPPLEMENTARY DATA

Supplementary Data are available at NAR Online.

ACKNOWLEDGEMENT

We thank Prof. Qingguo Gong, Dr Lijun Wang, Pengzhi Wu, Dr Fudong Li, Lingna Yang and Li Xu for helpful discussions; and Liyan Yu and Prof. Congzhao Zhou for help with the ITC experiments. We thank the staff of the Beamline BL17U at SSRF for assistance with data collection.

FUNDING

Strategic Priority Research Program of the Chinese Academy of Sciences [XDB08010100 and XDB08030302]; Research Program of the Chinese Academy of Sciences [KJZD-EW-L05]; Chinese National Natural Science Foundation [31330018]; China Postdoctoral Science Foundation [2015M582010]. Funding for open access charge: Strategic Priority Research Program of the Chinese Academy of Sciences [XDB08010100 and XDB08030302]; Research Program of the Chinese Academy of Sciences [KJZD-EW-L05]; Chinese National Natural Science Foundation [31330018]; China Postdoctoral Science Foundation [2015M582010].
Conflict of interest statement. None declared.

REFERENCES

1. Harigaya,Y., Tanaka,H., Yamanaka,S., Tanaka,K., Watanabe,Y., Tsutsumi,C., Chikashige,Y., Hiraoka,Y., Yamashita,A. and Yamamoto,M. (2006) Selective elimination of messenger RNA prevents an incidence of untimely meiosis. *Nature*, **442**, 45–50.
2. Yamanaka,S., Yamashita,A., Harigaya,Y., Iwata,R. and Yamamoto,M. (2010) Importance of polyadenylation in the selective elimination of meiotic mRNAs in growing S. pombe cells. *EMBO J.*, **29**, 2173–2181.
3. St-André,O., Lemieux,C., Perreault,A., Lackner,D.H., Bähler,J. and Bachand,F. (2010) Negative regulation of meiotic gene expression by the nuclear poly (a)-binding protein in fission yeast. *J. Biol. Chem.*, **285**, 27859–27868.
4. Chen,H.M., Futcher,B. and Leatherwood,J. (2011) The fission yeast RNA binding protein Mmi1 regulates meiotic genes by controlling intron specific splicing and polyadenylation coupled RNA turnover. *PLoS One*, **6**, e26804.
5. Yamashita,A., Takayama,T., Iwata,R. and Yamamoto,M. (2013) A novel factor Iss10 regulates Mmi1-mediated selective elimination of meiotic transcripts. *Nucleic Acids Res.*, gkt763.
6. Sugiyama,T. and Sugioka-Sugiyama,R. (2011) Red1 promotes the elimination of meiosis-specific mRNAs in vegetatively growing fission yeast. *EMBO J.*, **30**, 1027–1039.
7. Sugiyama,T., Wanatabe,N., Kitahata,E., Tani,T. and Sugioka-Sugiyama,R. (2013) Red5 and three nuclear pore components are essential for efficient suppression of specific mRNAs during vegetative growth of fission yeast. *Nucleic Acids Res.*, **41**, 6674–6686.
8. Yamashita,A., Shichino,Y., Tanaka,H., Hiriart,E., Touat-Todeschini,L., Vavasseur,A., Ding,D., Hiraoka,Y., Verdel,A. and Yamamoto,M. (2012) Hexanucleotide motifs mediate recruitment of the RNA elimination machinery to silent meiotic genes. *Open Biol.*, **2**, 120014.
9. Shichino,Y., Yamashita,A. and Yamamoto,M. (2014) Meiotic long non-coding meiRNA accumulates as a dot at its genetic locus facilitated by Mmi1 and plays as a decoy to lure Mmi1. *Open Biol.*, **4**, 140022.
10. Shah,S., Wittmann,S., Kilchert,C. and Vasiljeva,L. (2014) LncRNA recruits RNAi and the exosome to dynamically regulate *pho1* expression in response to phosphate levels in fission yeast. *Genes Dev.*, **28**, 231–244.
11. Ard,R., Tong,P. and Allshire,R.C. (2014) Long non-coding RNA-mediated transcriptional interference of a permease gene confers drug tolerance in fission yeast. *Nat. Comm.*, **5**, 5576.
12. Zofall,M., Yamanaka,S., Reyes-Turcu,F.E., Zhang,K., Rubin,C. and Grewal,S.I. (2012) RNA elimination machinery targeting meiotic mRNAs promotes facultative heterochromatin formation. *Science*, **335**, 96–100.
13. Hiriart,E., Vavasseur,A., Touat-Todeschini,L., Yamashita,A., Gilquin,B., Lambert,E., Perot,J., Shichino,Y., Nazaret,N., Boyaul,C. *et al.* (2012) Mmi1 RNA surveillance machinery directs RNAi complex RITS to specific meiotic genes in fission yeast. *EMBO J.*, **31**, 2296–2308.
14. Tashiro,S., Asano,T., Kanoh,J. and Ishikawa,F. (2013) Transcription-induced chromatin association of RNA surveillance factors mediates facultative heterochromatin formation in fission yeast. *Genes Cells*, **18**, 327–339.
15. Dominissini,D., Moshitch-Moshkovitz,S., Schwartz,S., Salmon-Divon,M., Ungar,L., Osenberg,S., Cesarkas,K., Jacob-Hirsch,J., Amariglio,N., Kupiec,M. *et al.* (2012) Topology of the human and mouse m^6A RNA methylomes revealed by m^6A-seq. *Nature*, **485**, 201–206.
16. Wang,X., Lu,Z., Gomez,A., Hon,G.C., Yue,Y., Han,D., Fu,Y., Parisien,M., Dai,Q., Jia,G. *et al.* (2014) N^6-methyladenosine-dependent regulation of messenger RNA stability. *Nature*, **505**, 117–120.
17. Wang,X., Zhao,B.S., Roundtree,I.A., Lu,Z., Han,D., Ma,H., Weng,X., Chen,K., Shi,H. and He,C. (2015) N^6-methyladenosine modulates messenger RNA translation efficiency. *Cell*, **161**, 1388–1399.
18. Xu,C., Wang,X., Liu,K., Roundtree,I.A., Tempel,W., Li,Y., Liu,Z., He,C. and Min,J. (2014) Structural basis for selective binding of m^6A RNA by the YTHDC1 YTH domain. *Nat. Chem. Biol.*, **10**, 927–929.
19. Schwartz,S., Agarwala,S.D., Mumbach,M.R., Jovanovic,M., Mertins,P., Shishkin,A., Mertins,P., Ter-Ovanesyan,D., Habib,N., Cacchiarelli,D. *et al.* (2013) High-resolution mapping reveals a conserved, widespread, dynamic mRNA methylation program in yeast meiosis. *Cell*, **155**, 1409–1421.
20. Luo,S. and Tong,L. (2014) Molecular basis for the recognition of methylated adenines in RNA by the eukaryotic YTH domain. *Proc. Natl. Acad. Sci. U.S.A.*, **111**, 13834–13839.
21. Theler,D., Dominguez,C., Blatter,M., Boudet,J. and Allain,F.H.T. (2014) Solution structure of the YTH domain in complex with N^6-methyladenosine RNA: a reader of methylated RNA. *Nucleic Acids Res.*, **42**, 13911–13919.
22. Li,F., Zhao,D., Wu,J. and Shi,Y. (2014) Structure of the YTH domain of human YTHDF2 in complex with an m^6A mononucleotide reveals an aromatic cage for m^6A recognition. *Cell Res.*, **24**, 1490–1492.
23. Zhu,T., Roundtree,I.A., Wang,P., Wang,X., Wang,L., Sun,C., Tian,Y., Li,J., He,C. and Xu,Y. (2014) Crystal structure of the YTH domain of YTHDF2 reveals mechanism for recognition of N^6-methyladenosine. *Cell Res.*, **24**, 1493–1496.
24. Xu,C., Liu,K., Ahmed,H., Loppnau,P., Schapira,M. and Min,J. (2015) Structural basis for the discriminative recognition of N6-methyladenosine RNA by the human YT521-B homology domain family of proteins. *J. Biol. Chem.*, **290**, 24902–24913.
25. Vagin,A. and Teplyakov,A. (2009) Molecular replacement with MOLREP. *Acta Crystallogr. D Biol. Crystallogr.*, **66**, 22–25.
26. Murshudov,G.N., Skubák,P., Lebedev,A.A., Pannu,N.S., Steiner,R.A., Nicholls,R.A., Winn,M.D., Long,F. and Vagin,A.A. (2011) REFMAC5 for the refinement of macromolecular crystal structures. *Acta Crystallogr. D Biol. Crystallogr.*, **67**, 355–367.
27. Emsley,P., Lohkamp,B., Scott,W.G. and Cowtan,K. (2010) Features and development of Coot. *Acta Crystallogr. D Biol. Crystallogr.*, **66**, 486–501.
28. DeLano,W.L. (2002) ThePyMOLMolecular Graphics System. *DeLano Scientific*. San Carlos.
29. Engel,J.D. and Von Hippel,P.H. (1974) Effects of methylation on the stability of nucleic acid conformations. Monomer level. *Biochemistry*, **13**, 4143–4158.
30. Roost,C., Lynch,S.R., Batista,P.J., Qu,K., Chang,H.Y. and Kool,E.T. (2015) Structure and thermodynamics of N^6-methyladenosine in

RNA: a spring-loaded base modification. *J. Am. Chem. Soc.*, **137**, 2107–2115.
31. Fu,Y., Dominissini,D., Rechavi,G. and He,C. (2014) Gene expression regulation mediated through reversible m^6A RNA methylation. *Nat. Rev. Genet.*, **15**, 293–306.
32. Bujnicki,J.M., Feder,M., Radlinska,M. and Blumenthal,R.M. (2002) Structure prediction and phylogenetic analysis of a functionally diverse family of proteins homologous to the MT-A70 subunit of the human mRNA: m^6A methyltransferase. *J. Mol. Evol.*, **55**, 431–444.